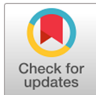

Research Article | Vol. 26, No. 17 | 20 Aug 2018 | OPTICS EXPRESS 22218

Optics EXPRESS

Printing sub-micron structures using Talbot mask-aligner lithography with a 193 nm CW laser light source

ANDREAS VETTER,[1,2,*] RAOUL KIRNER,[1] DMITRIJS OPALEVS,[3] MATTHIAS SCHOLZ,[3] PATRICK LEISCHING,[3] TORALF SCHARF,[4] WILFRIED NOELL,[1] CARSTEN ROCKSTUHL,[2,5] AND REINHARD VOELKEL[1]

[1]*SUSS MicroOptics SA, Rouges-Terres 61, CH-2068 Hauterive, Switzerland*
[2]*Institute of Nanotechnology, Karlsruhe Institute of Technology, Hermann-von-Helmholtz-Platz 1, 76344 Eggenstein-Leopoldshafen, Germany*
[3]*TOPTICA Photonics AG, Lochhamer Schlag 19, 82166 Gräfelfing, Germany*
[4]*Nanophotonics and Metrology Laboratory, École Polytechnique Fédérale de Lausanne, CH-1015 Lausanne, Switzerland*
[5]*Institute of Theoretical Solid State Physics, Karlsruhe Institute of Technology, Wolfgang-Gaede-Strasse 1, 76131 Karlsruhe, Germany*
[*]*andreas.vetter@suss.com*

Abstract: A continuous improvement of resolution in mask-aligner lithography is sought after to meet the requirements of an ever decreasing minimum feature size in back-end processes. For periodic structures, utilizing the Talbot effect for lithography has emerged as a viable path. Here, by combining the Talbot effect with a continuous wave laser source emitting at 193 nm, we demonstrate successfully the fabrication of periodic arrays in silicon substrates with sub-micron feature sizes. The excellent coherence and the superior brilliance of this light source, compared to more traditional mercury lamps and excimer lasers as light source, enables the efficient beam shaping and a reduced minimum feature size at a fixed gap of 20 µm. We present a comprehensive study of proximity printing with this system, including simulations and selected experimental results of prints in up to the fourth Talbot plane. This printing technology can be used to manufacture optical metasurfaces, bio-sensor arrays, membranes, or microchannel plates.

© 2018 Optical Society of America under the terms of the OSA Open Access Publishing Agreement

1. Introduction

In the 1960s, mask-aligners emerged as a viable tool for high-volume fabrication. Mask-aligner lithography relies on the pattern transfer via shadow printing of mask structures, in general possessing a complex transmission function, to a photoresist-coated wafer. While the best resolution is achieved in contact between mask and wafer, in practice proximity lithography with a certain gap g is preferred. In this *modus operandi*, contamination of the mask is prevented, avoiding abundant mask cleaning that results in an increased yield [1]. The lower bound for the proximity gap depends on the flatness of mask and wafer, as well as on the height of prestructured patterns on the substrate, and typically amounts to about 20 µm.

In the 1980s, the ongoing miniaturization trend in semiconductor technology required the fabrication of sub-micron structures using optical lithography, and thus prompted the use of projection lithography. However, mask-aligners remain until today the tool of choice to pattern uncritical layers in the semiconductor back-end, e.g., for light-emitting diode (LED) manufacturing and for electrical interconnects in fan-outs. Mask-aligners offer greatly reduced complexity and cost in investment and operation over steppers used in projection lithography, rendering them the tool of choice for uncritical back-end patterning.

The main effect limiting the resolution in proximity printing is diffraction at mask structures,

#332512 https://doi.org/10.1364/OE.26.022218
Journal © 2018 Received 4 Jun 2018; revised 13 Jul 2018; accepted 21 Jul 2018; published 13 Aug 2018

affecting the subsequent image transfer over the proximity gap g [2]. The resolution at a wavelength λ can be estimated to be [3]

$$\text{Resolution} \sim \sqrt{\lambda \cdot g}\,. \tag{1}$$

The resolution in mask-aligner lithography is indicated in Fig. 1(a) for two different gap sizes of 20 µm and 40 µm as a function of wavelength. An obvious approach to enhance the resolution is to reduce the proximity gap, with mask and wafer in contact as the extreme case. However, as described before, reducing the proximity gap below some tens of micron is not a practical solution for high-volume fabrication.

Hence, there are two ways to improve the resolution in mask-aligner lithography for a fixed proximity gap. The first is evident and concerns the use of light sources with ever smaller wavelengths [compare Fig. 1(a)]. Traditionally, light sources such as mercury high-pressure arc lamps or pulsed excimer laser lasers have been used for this purpose [4]. However, they suffer from multiple problems and recently light emitting diodes or laser diodes as continuous wave (CW) sources in the deep-ultraviolet (DUV) spectral regions were established as light sources used in lithography. These novel light sources excel in terms of luminous efficacy, maintenance requirements, environmental sustainability, wall-plug efficiency, and demands on cooling effort [5].

The integration of LED and diode laser light sources into mask-aligner lithography has been demonstrated [6–8], solving the task of beam shaping for uniform mask illumination in various ways. Recently, we reported on the implementation of a novel deep ultraviolet (DUV) frequency-quadrupled continuous wave (CW) light source emitting at $\lambda = 193$ nm in a mask-aligner and demonstrated test exposures [9].

For periodic structures, a second further improvement of the attainable resolution in proximity lithography is possible by exploiting the Talbot effect. Under plane wave illumination in the Fresnel regime, the diffraction at laterally periodic mask features leads to their self-imaging and replication in a distance termed the Talbot distance z_{T} [10–12] (see Section 2). By locating the resist-coated substrate in one of the Talbot planes, the mask design is replicated [13–15], achieving a considerably improved resolution over conventional proximity lithography, as described by Eq. (1). Several developments in the realm of Talbot lithography have been reported, including displacement [16], immersion [17], and gray-scale Talbot lithography [18].

In general, a standard mask-aligner setup is sufficient to perform Talbot lithography. But two important technical requirements have to be fulfilled. First, to prevent lateral image blurring in the Talbot plane, collimated near plane wave illumination is required for the exposure [1]. Thus, a laser source is most suitable, since its high brilliance allows efficient beam shaping for the generation of collimated light. And second, the gap between mask and photoresist-coated wafer has to be set precisely, in order to place the wafer in one of the Talbot planes to maximize the contrast of self-imaging. Whereas the second property is rather a practical constraint, the first requirement can be satisfied only with the recently introduced frequency-quadrupled CW laser light source that has a very high brilliance. Hence, the availability of such source prompts for its use in the printing of sub-micron features of periodic structures exploiting the Talbot effect. In addition, the reduction of the wavelength over traditional light sources leads to a decrease in the minimum feature size for a fixed proximity gap.

Here, we demonstrate the benefits of exploiting this light source for printing with the Talbot effect for the self-imaging of periodic mask structures, making use of the coherent nature of the light source. Following this methodology, periodic patterns with sub-micron feature size are demonstrated at a comparably large proximity gap, suited for high-volume nano- and microfabrication.

In the following Section 2, we provide for completeness a short derivation of the Talbot effect within the angular spectrum method (ASM), and elaborate why a reduction in wavelength is

Optics EXPRESS

likewise beneficial for Talbot lithography. In Section 3, the optical setup and the laser beam shaping for collimated near plane wave illumination are discussed, also including the mitigation of speckle patterns in the photoresist emerging from the high coherence of the laser source. Subsequently, the simulation of Talbot structures is discussed in Section 4, also addressing reflections at silicon (Si) substrates, as used for experimental verification. The results of Talbot lithography with a laser source emitting at 193 nm are presented in Section 5. We conclude and finalize on our work in a devoted Section 6.

2. Theory of Talbot lithography

The classical Talbot effect describes the self-imaging of longitudinally periodic structures [10]. The distance between planes in which the field replicates itself is given by the Talbot distance z_T, while the depth of focus (DOF) denotes the length scale across which self-imaging occurs with high contrast. Both quantities will be derived in the following within the scalar approximation for a periodic structure [12, 19, 20]. Based on these results, we discuss the implications for Talbot lithography in the DUV.

Starting point is the complex field distribution $p(\mathbf{r})$ behind the periodic structure. In thin-element approximation, which we assume here, it is given by the product of the incident field and the complex transmission function of the structure. The position of each unit cell of the periodic object is described by the linear combination

$$\mathbf{a_n} = n_1\mathbf{a}_1 + n_2\mathbf{a}_2 \tag{2}$$

of the basis vectors $\mathbf{a}_1$ and $\mathbf{a}_2$ in the two-dimensional object plane, with integers n_1 and n_2. The periodic field of the object $p(\mathbf{r}) = p(\mathbf{r} + \mathbf{a_n})$ is described by the set $\{\mathbf{a_n}\}$. The reciprocal lattice vectors $\mathbf{b}_{1,2}$ are given via $\mathbf{a}_\mathrm{i} \cdot \mathbf{b}_\mathrm{j} = \delta_\mathrm{ij}$.

Assuming plane wave illumination, the field behind the object in thin-element approximation can be written as a function of its 2D Fourier coefficients $P_\mathbf{n}$,

$$p(\mathbf{r}) = \sum_\mathbf{n} P_\mathbf{n} \exp\left(2\pi i\, \mathbf{r} \cdot \mathbf{b_n}\right), \tag{3}$$

with the summation over all pairs $\mathbf{n} = (n_1, n_2)$.

We proceed by writing the transfer function or propagator $H(|\mathbf{b_n}|, z)$ of wave propagation along a distance z at wavelength λ, using the angular spectrum method (ASM) for plane waves [21]. This approach is equivalent to the first Rayleigh-Sommerfeld solution [22].

$$H(|\mathbf{b_n}|, z) = \begin{cases} \exp\left[i2\pi \frac{z}{\lambda}\sqrt{1-(\lambda\,|\mathbf{b_n}|)^2}\,\right], & |\mathbf{b_n}| < \frac{1}{\lambda} \\ 0, & \text{otherwise.} \end{cases} \tag{4}$$

The diffracted field distribution behind the object is obtained within the ASM under plane wave illumination with a unitary amplitude as [21]

$$u_\mathrm{diff}(x, y, z) = \iint \tilde{p}(\mathbf{b_n}; z = 0)\, H(|\mathbf{b_n}|, z)\, \exp\left(2\pi i\, \mathbf{r} \cdot \mathbf{b_n}\right) d\mathbf{r}, \tag{5}$$

with

$$\begin{aligned} \tilde{p}(\mathbf{b_n}; z = 0) &= \iint p(\mathbf{r}) \exp\left(-2\pi i\, \mathbf{r} \cdot \mathbf{b_n}\right) d\mathbf{r} \\ &= \sum_\mathbf{n} P_\mathbf{n} \end{aligned} \tag{6}$$

Optics EXPRESS

the Fourier transform of the transmitted electric field directly behind the object under thin-element approximation, with $p(\mathbf{r})$ from Eq. (3). The necessary and sufficient condition for self-imaging can be retrieved from Eq. (5): The original field, as defined by Eq. (3), is reproduced in certain Talbot planes at the Talbot distance z_T, if the phase difference between the zeroth order and the diffracted field according to Eq. (4) for the periodic structure vanishes, i.e.

$$\exp\left[i2\pi\frac{z_\mathrm{T}}{\lambda} - i2\pi\frac{z_\mathrm{T}}{\lambda}\sqrt{1-(\lambda\,|\mathbf{b_n}|)^2}\right] \stackrel{!}{=} 1\,. \tag{7}$$

Then, the phase accumulation in each diffraction order is the same at these distances and the initial field simply replicates itself. This condition leads to a Talbot distance z_T of

$$z_\mathrm{T} = \frac{m\cdot\lambda}{1-\sqrt{1-(\lambda\,|\mathbf{b_n}|)^2}} \qquad m\in\mathbb{N}\,. \tag{8}$$

For simplicity and out of experimental relevance, we restrict the further discussion to bi-periodic structure with period Λ in each dimension. Inserting $|\mathbf{b_n}| = {}^1/_\Lambda$ and $m = 1$ in Eq. (8), the condition for the first Talbot plane is obtained. This result is equal to the findings already contained in the first publication on the Talbot effect [10].

The Talbot distance according to Eq. (8) is plotted in Fig. 1(b) as a function of wavelength for periods of $\Lambda = 1.39\,\mu\mathrm{m}$ and $0.71\,\mu\mathrm{m}$, respectively. At an illumination wavelength of 193 nm, this corresponds to a Talbot distance of 20 µm and 5 µm for the first Talbot plane, respectively.

For typical applications in mask-aligner lithography, the period of the structure is larger than the wavelength, ${}^1/_{|\mathbf{b_n}|} \gg \lambda$, and Eq. (8) can be simplified by applying a binomial expansion of the

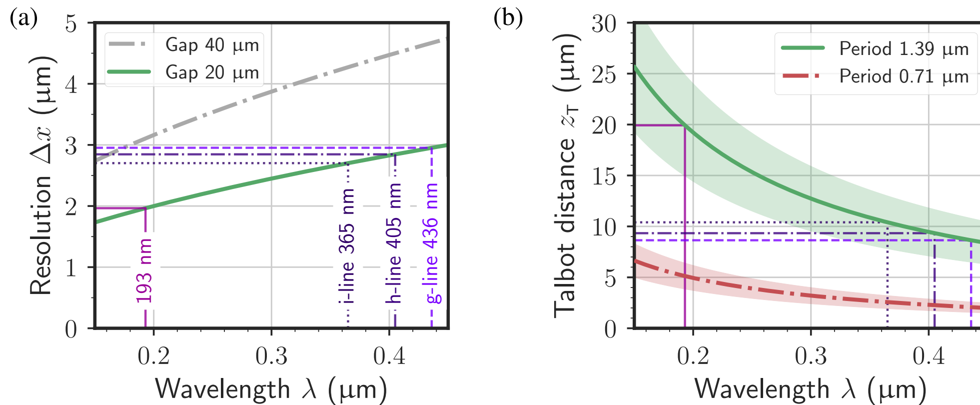

Fig. 1. (a) Lateral resolution in mask-aligner lithography as a function of wavelength, according to Eq. (1). Vertical lines indicate the crucial wavelengths for mask-aligner illumination. For illustration, the resolution is shown for a gap of 20 µm (as used throughout the experiments) and 40 µm. The resolution improves for smaller wavelengths and gaps, with a value of $\sim 2\,\mu\mathrm{m}$ at a gap of 20 µm under illumination at 193 nm [9]. (b) Talbot distance z_T as a function of wavelength for two relevant periods Λ, according to Eq. (8). The DOF is indicated by the color shaded areas [Eq. (13)]. The highlighted wavelengths correspond to the annotations in (a). The DOF scales with the Talbot distance for a fixed period. Accordingly, the DOF and hence the process window increases for our light source, compared to canonical high-pressure mercury lamps (g, h, and i-lines). The different Talbot distances for the emission lines of mercury lamps lead to a spectral blur for broadband illumination.

square root:

$$\sqrt{1-(\lambda\,|\mathbf{b_n}|)^2} \simeq 1-\tfrac{1}{2}(\lambda\,|\mathbf{b_n}|)^2\,. \tag{9}$$

Within this approximation, the condition for self-imaging under plane wave illumination in Eq. (8) is simplified to

$$z_\mathrm{T} \simeq 2m\frac{\Lambda^2}{\lambda}\,. \tag{10}$$

This approach is equivalent to the Fresnel approximation, as can be seen by applying the binomial expansion of Eq. (9) to Eq. (4),

$$H_\mathrm{Fresnel}(|\mathbf{b_n}|, z) = \exp\left[i2\pi\frac{z}{\lambda}\left\{1-\tfrac{1}{2}\lambda^2\,|\mathbf{b_n}|^2\right\}\right], \tag{11}$$

and repeating the steps of Eqs. (5) to (8). However, throughout this publication, the more exact Eq. (8) is used for calculating the lateral periods of the mask patterns, both in simulations and experiments.

The DOF in Talbot proximity lithography can be retrieved in analogy to projection lithography as a function of wavelength λ and numerical aperture (NA) of the optical system [15, 23, 24]

$$\mathrm{DOF} \approx \pm\frac{\lambda}{2(\mathrm{NA})^2} = \pm\frac{\lambda}{2(n\cdot\sin\theta)^2}, \tag{12}$$

with the diffraction angle θ and the refractive index n of the immersion medium (here air, $n = 1$). The diffraction at the periodic pattern leads to an angular spread, given by $\sin\theta = \frac{\lambda}{(n\cdot\Lambda)}$. Using Eq. (10), this leads to a DOF of

$$\mathrm{DOF} \approx \pm\frac{\Lambda^2}{2\lambda} = \pm\frac{z_\mathrm{T}}{4}\,. \tag{13}$$

The benefits of using an exposure source with a reduced wavelength compared to i-line illumination at 365 nm, as presented here with a frequency-quadrupled laser emitting at 193 nm, are evident from Eqs. (10) and (13), as depicted in Fig. 1(b): For a fixed period, the Talbot distance increases, relaxing the constraint of small gap sizes. Conversely, for a fixed Talbot distance, in our case at the proximity gap of 20 µm, the lateral period Λ scales with $\sqrt{\lambda}$ [the same behavior as observed in Eq. (1)]. Thus, by decreasing the wavelength from 365 nm to 193 nm, the lateral period Λ for the Talbot effect can be reduced by a factor of about 1.38, while keeping the proximity gap and therefore the mechanical mask-aligner setup fixed.

Following Eq. (13), the DOF scales with the Talbot distance, and thus increases with decreasing wavelength as well [compare Fig. 1(b)]. Hence, the process window regarding a variation of the proximity gap is increased. Most interestingly, in projection lithography this trend is reversed. According to Eq. (12), the DOF scales with the wavelength for a fixed NA, reducing the process window.

In addition, the sharp spectral linewidth of the laser source prevents a spectral blur of the Talbot distance, which can be observed for the different emission lines of high-pressure mercury lamps [compare Fig. 1(b)]. On the basis of the laser's high brilliance, efficient beam shaping for near plane wave illumination can be achieved, which will be discussed in the following section.

3. Optical setup and beam shaping

A schema of the optical setup for the mask-aligner illumination is shown in Fig. 2. It can be separated into two parts, namely, DUV light generation [Fig. 2(a)] and laser beam shaping [Fig. 2(b)].

The light source consists of a seed diode laser, emitting at 772 nm, and a subsequent power amplification stage using a tapered amplifier (TA) in master-oscillator power-amplifier (MOPA) configuration [25, 26]. Two bow-tie second-harmonic generation (SHG) cavities, stabilized by

Optics EXPRESS

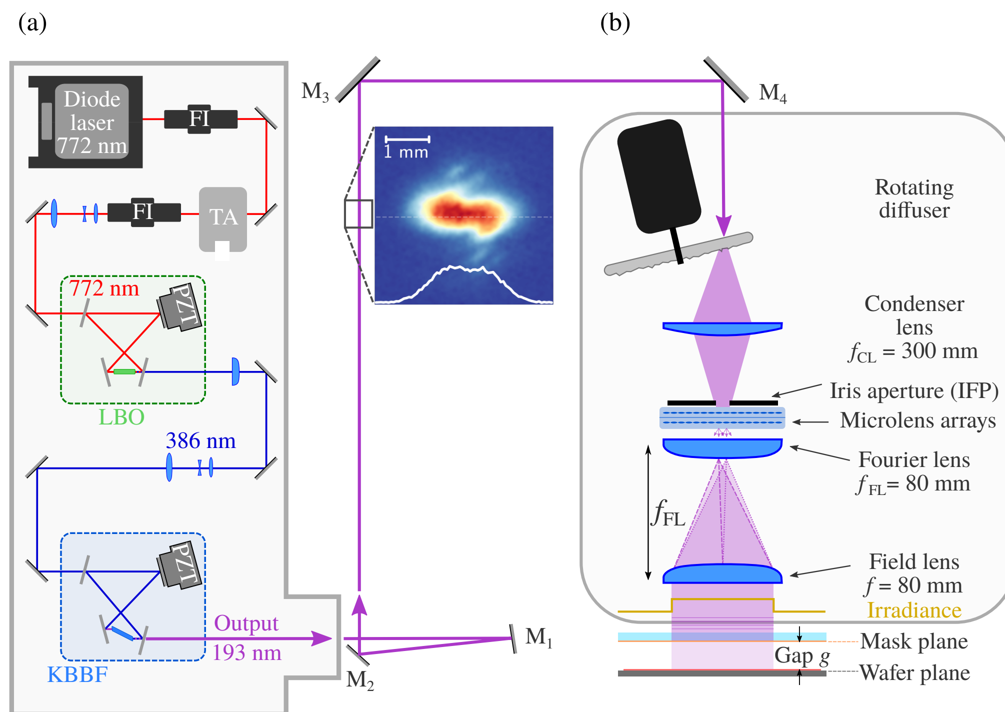

Fig. 2. (a) Schematic of the CW laser source emitting at 193 nm. The light of a diode seed laser is directed through a Faraday isolator (FI) and enhanced in a tapered amplifier (TA). Behind a second FI, the frequency upconversion is performed in lithium triborate (LBO) and potassium fluoro-beryllo-borate (KBBF) nonlinear crystals. For stable operation, an active feedback control is integrated using piezo elements (PZTs). The inset shows the beam profile before homogenization. Adapted from [25]. (b) Optical setup for beam homogenization. A uniform flat-top illumination in the mask plane is obtained by using a rotating diffuser and a Köhler integrator, consisting of microlens arrays (MLAs), Fourier, and field lenses. An iris aperture is used as an illumination filter plate (IFP) to control the angular spectrum.

the Pound-Drever-Hall technique [27], frequency-quadruple the output of the TA to the target wavelength of 193 nm. The first stage contains a lithium triborate (LBO) nonlinear crystal, performing the upconversion to an intermediate wavelength of 386 nm. The further upconversion is accomplished in a second stage using a potassium fluoro-beryllo-borate (KBBF) crystal, optically bonded between CaF_2 prisms to access the correct crystal plane for phase matching. The spectral linewidth of the optical output after the frequency upconversion is about 100 kHz and thus orders of magnitude smaller than for excimer lasers [28]. With this industrial grade laser setup, an optical output power up to 20 mW is possible. Including a KBBF crystal shifter in combination with automated alignment routines, lifetimes up to 10 000 hours for an output power of 10 mW are within reach [26]. In comparison, excimer laser sources for mask-aligner lithography have been demonstrated with an optical power of 7.5 W at 193 nm [4]. Weichelt *et al.* reported on a pulsed solid-state laser source with an optical power of 3 W and emitting at a wavelength of 355 nm [7].

The laser output exhibits an elliptical beam profile, as depicted in the inset of Fig. 2(a). Further

homogenization is required to obtain a uniform flat-top distribution in the mask plane [29, 30]. Furthermore, the high coherence of the laser source manifests itself in interference effects, typically unintended in high-resolution lithography. The main effect consists of speckle formation in the photoresist, which has to be mitigated in its impact. Another requirement for Talbot lithography is near plane wave illumination, as discussed in Sections 2 and 4.

To take all the aforementioned constraints into account, a combination of rotating diffuser and imaging homogenizer is applied [see Fig. 2(b)]. First, a shaped random diffuser, consisting of concave facets of similar curvature but arbitrary size, is inserted into the beam path. For a fixed configuration of these facets, speckle form in the resist plane. By rotating the diffuser during the exposure, the irradiance of various statistically independent speckle patterns is integrated in the resist during exposure. The superposition of these patterns reduces the visibility of speckle, as demonstrated later in this section [9, 31–33].

Uniform irradiance in the mask plane is achieved using an imaging microlens array (MLA) homogenizer as a Köhler integrator, i.e., a combination of two MLAs and a Fourier lens [34]. In comparison to a previous approach using a diffractive non-imaging homogenizer [9], we demonstrate here a clear improvement with regard to field uniformity and light efficiency [33]. Though the results of this publication are limited to small print fields of about 15 mm x 15 mm to maintain reasonable exposure times for the proof-of-principle experiments, the demonstrated principles can be directly adapted to full-field mask-aligner illumination.

We use in our configuration two arrays of microlenses [see Fig. 2(b)], which are separated by one focal distance. One single MLA is constructed from cylindrical microlenses, with a pitch of 300 µm, on both sides of a fused silica substrate. A crossed assembly of two MLAs results in a square flat-top illumination in the mask plane [31]. In addition, a field lens identical to the Fourier lens and in focal distance to it guarantees telecentric illumination.

As depicted in Fig. 2(b), the Fourier lens performs a Fourier transform, i.e., converting the illuminated area on the MLA to an angular spectrum in the mask plane. By strongly reducing this area on the first MLA, illumination with very small angles is obtained. This principle allows to control the angular distribution of the illumination in the mask plane at will, and is typically implemented as tandem Köhler integrators in modern mask-aligners (MO Exposure Optics [35]): By arranging two integrators in sequence, the first integrator ensures a uniform illumination of the second integrator, resulting in a uniform irradiance and uniform angular spectrum in the mask plane. Here, we rely only on a single integrator, reducing the number of optical elements in the beam path and thus increasing the light efficiency. This is possible since we are only interested in obtaining a narrow angular spectrum, which is not required to be uniform. A further gain in light yield can be obtained using anti-reflective coatings for the optical elements in the beam path.

In our optical setup, we use an iris aperture as illumination filter plate (IFP) to selectively block transmission except for channels close to the optical axis, restricting the angular spectrum to near plane wave illumination. However, to achieve uniform illumination in the mask plane, a minimum number of channels is required to mix the incident light. This represents the fundamental trade-off for plane wave illumination with imaging homogenizers, between a narrow angular spectrum and a uniform field distribution in the mask plane.

Simulations and measurements of the implemented illumination in the mask plane [see Fig. 2(b)] are shown in Fig. 3. Incoherent ray-tracing simulations are performed using Zemax OpticsStudio. The power uniformity and the angular spectrum of the illumination in the mask plane is measured by scanning a UV-sensitive photodiode (Hamamatsu S1226-18BQ Si photodiode, photosensitivity 0.13 A W^{-1} @ 193 nm) over the area of interest. The optically active area, defining the lateral sampling, is limited to 300 µm x 300 µm by a laser-cut aperture. A xy-stage with micron precision is used for scanning the diode, with a step size of 300 µm. For each scan position, we average over 20 measurements with an individual integration time of 10 ms. This procedure ensures repeatable results, as confirmed by multiple measurements. In

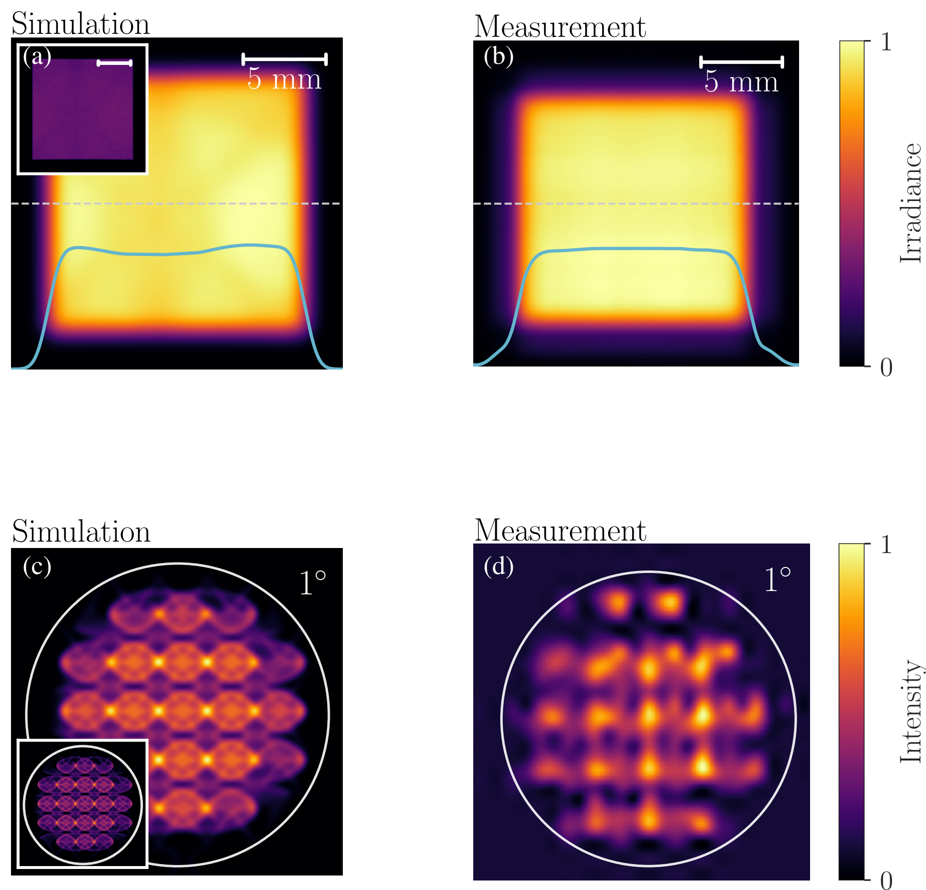

Fig. 3. (a) Simulated and (b) measured flat-top irradiance distribution in the mask plane, with the irradiance profile along the dashed line depicted in white. The simulated pixels are convoluted with a Gaussian filter, corresponding to the size of the aperture used in the measurement. The experimentally determined non-uniformity is below 3 %. The insets show the data without filtering. (c) Simulated and (d) measured intensity distribution of the angular spectrum. The angular spectrum is retrieved in the mask plane [see Fig. 2(b)]. Due to under-filling of the MLA's acceptance angles, individual microlens channels are visible. The maximum half-angles in (d) are below 1° (white circle). The presented data in (b) and (d) is identical to the measurements included in [36], here completed by simulation results.

order to compare simulation and measurement, the simulated data is sampled with a Gaussian filter, with a standard deviation equal to the aperture size.

For a field size of about 15 mm x 15 mm, a highly uniform irradiance distribution is simulated and confirmed by measurement, with a measured non-uniformity below 3 %. This value is comparable to the canonical MO Exposure Optics for beam homogenization [35,37], meeting the requirement for proximity lithography. Please note that the field size in our proof-of-principle experiment is limited to the size of the test structures on our mask and can be extended with ease

Optics EXPRESS

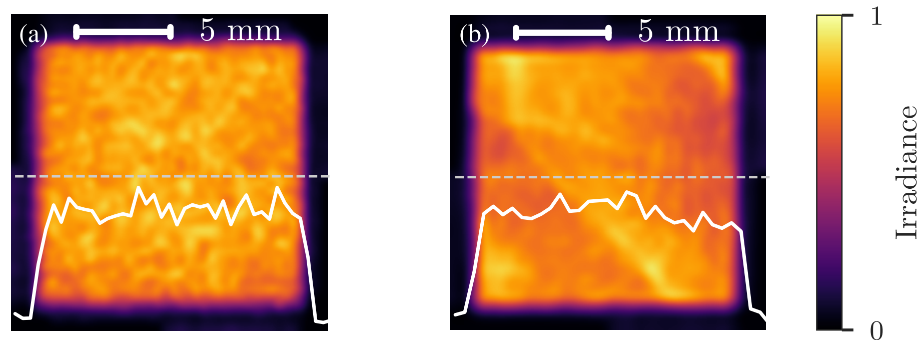

Fig. 4. Measured irradiance distribution in the mask plane for (a) static and (b) without diffuser. For both configurations, the formation of speckle is visible. The irradiance profile along the dashed line is depicted in white. Compared to Fig. 3(b), the uniformity is greatly diminished.

to full wafer size by adapting the numerical aperture of the MLAs and the focal length f_{FL} of the Fourier lens.

The angular spectrum of the illumination setup is obtained by inserting a lens in the mask plane (uncoated fused silica, plano-convex, $f \simeq 125$ mm at $\lambda = 193$ nm) and measuring the intensity in the focal plane of this lens. We compare simulation and measurement in Fig. 3(c) and Fig. 3(d), respectively. Because of under-filling of the MLAs' NA, individual microlens channels become visible. The half-angles of each channel are below 1°, in good agreement between simulation and measurement, and correspond to a well-collimated beam suitable for Talbot lithography.

To demonstrate the importance of the rotating shaped random diffuser for beam shaping, we depict the measured irradiance distribution of our optical setup for a static [Fig. 4(a)] and without a diffuser [Fig. 4(b)] in the beam path [compare Fig. 2(b)]. Speckle are clearly visible in both configurations, and the non-uniformity is strongly increased.

4. Aerial image and resist simulation

In order to assess the field profile behind the periodic features of a chromium amplitude mask, we perform a simulation of our exposure system using LayoutLab from GenISys [38], a software dedicated to process optimization and development in optical lithography. Wave propagation is calculated by solving the Rayleigh-Sommerfeld diffraction integral, taking into account the stack of materials (air, resist, Si substrate) using the transfer matrix method (TMM).

Figure 5 shows the propagating field behind the mask, i.e., the irradiance distribution in air, plotted over two Talbot distances. In Fig. 5(a), the simulation is shown for idealized plane wave illumination, while Fig. 5(b) shows the results using the angular spectrum measurement depicted in Fig. 3(d) as input. As described before, the deviation from perfect plane wave illumination leads to the observed lateral blurring, likewise diminishing the contrast. Indeed, the circular shape of the periodic mask features is reproduced in the first Talbot plane, demonstrating the operating principle under the actual illumination conditions.

In addition, multiple reflections occurring at the interfaces air/resist and resist/Si substrate leads to interference and the formation of standing waves along the propagation direction in the photoresist [39, 40]. At normal incidence at $\lambda = 193$ nm, the reflectance R at the interface

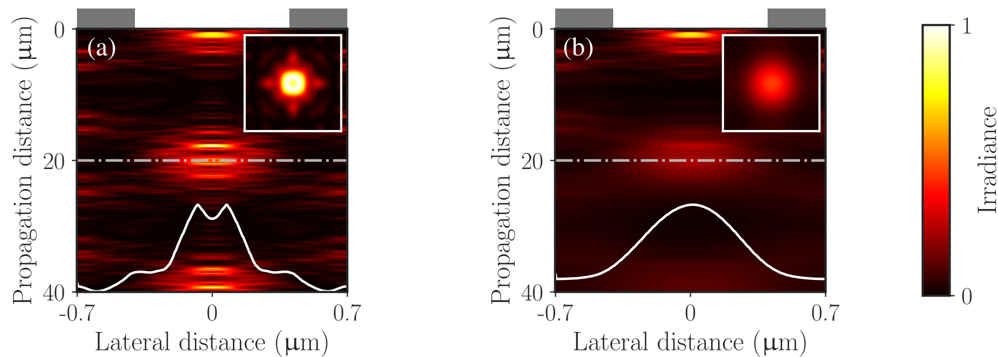

Fig. 5. Simulation of the propagating field behind the mask, under (a) plane wave illumination and (b) taking the measured angular spectrum, as shown in Fig. 3(d), into account. The irradiance is plotted in the middle of the unit cell along the propagation direction. Please note the different length scales on the axes. The periodic mask design contains an open circle (diameter 0.8 µm) in an otherwise opaque square unit cell (side length 1.4 µm, indicated in gray). The profile in the Talbot plane at $z_T = 20\,\mu m$ (along the dash-dotted line) is plotted in white. The insets show the irradiance in the Talbot plane. As expected, the circular feature shape is replicated, with a lateral blurring arising from the finite angular spectrum. The irradiance is normalized to the maximum in simulation (a).

air/resist amounts to about 6 % and to about 56% at the interface resist/Si. This is visible in Fig. 6(a), which shows the simulated irradiance distribution in 120 nm thick photoresist on top of a semi-infinite Si substrate. Detailed information on the optical properties of the resist can be requested from the supplier.

A bottom anti-reflective coating (BARC) can be applied between resist and substrate to diminish the reflection and therefore avoiding the formation of standing waves in the resist. This is demonstrated in the simulation depicted in Fig. 6(b), which includes a 78 nm thick BARC layer (ARC 25 from BrewerScience, Inc., $n_{\mathrm{BARC}} = 1.84 + 0.46\,i$). The material properties and the resist thickness is optimized for the wavelength under consideration. A great improvement in the uniformity of light distribution inside the resist is observed, and the formation of standing waves is strongly reduced.

However, in our proof-of-principle experiment, we had to refrain from applying a BARC due to the unavailability of suitable coatings in our laboratory. In general, using a BARC will lead to both a reduced variation of structure sizes and a smoother resist sidewall profile [41].

5. Experimental results of Talbot lithography

5.1. Methods

With the insights from Section 4, we proceed by presenting lithographic prints. We first describe the experimental details concerning the mechanical setup, resist chemistry, and pattern transfer via etching.

Apart from the optical setup depicted in Fig. 2(a), our mask-aligner system consists of a wafer chuck mounted on a high precision stage (Etel Sarigan) and a mask chuck. The proximity gap between mask and wafer is determined at three individual spots using a spectroscopic

Optics EXPRESS

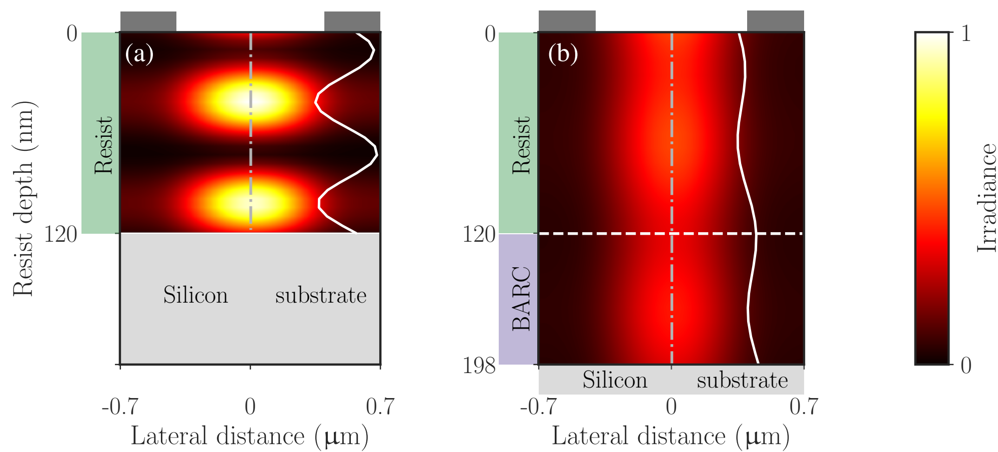

Fig. 6. Resist simulation for a proximity gap of $g = 20\,\mu\text{m}$ (not shown in the graph). The simulation (a) without bottom anti-reflective coating (BARC) shows irradiance hotspots arising from standing waves, while the application of a BARC (b) results in improved uniformity in the resist. The irradiance distribution along the gray dash-dotted line is plotted in white. The exposure conditions are identical to the simulation in Fig. 5(b). The graph is not to scale, please note the different length scales on the axes. The irradiance is normalized to the maximum irradiance in (a).

reflectometer in combination with a Fast Fourier Transform method (Avantes AvaSpec ThinFilm bundle). We use the retrieved values as a feedback to the stage in order to level the wafer with respect to the mask and to set a gap of 20 μm.

Regarding resist chemistry, a standard process for ArF excimer lithography is adapted (positive photoresist TOK TARF-P6239 ME, prebake and post-exposure bake 1 min at 110 °C, resist thickness 120 nm, development 1 min in AZ MIF 327). The exposure dose used in the presented prints amounts to 65 mJ cm^{-2}.

The chromium amplitude mask containing the periodic structures is fabricated using electron beam lithography. The resist pattern after development is used for a chromium lift-off process, generating a hardmask for subsequent reactive-ion etching (RIE) (24 sccm HBr and 12 sccm Cl_2, 150 W, Oxford Plasma Technology Plasmalab 100 ICP180).

5.2. First Talbot plane

It is important to note that the presented results aim for a 1:1 replication of the mask structures in the photoresist. No magnification or demagnification is intended. Furthermore, we restrict the experimental prints presented here to square periodic arrays with openings in the shape of simple geometries, i.e., triangles, squares, and circles. Especially the latter design is of interest for the high-volume fabrication of polarization-insensitive dielectric metasurfaces with high efficiency in the near- and mid-infrared [42–44].

First, we demonstrate the fabrication of rather large structures, by using the self-replication of periodic quadratic arrays with a period of $\Lambda = 2\,\mu\text{m}$. Following Eq. (8), this corresponds for our fixed proximity gap of $g = 20\,\mu\text{m}$ to $m = \frac{1}{2}$. The self-replication takes place in the first intermediate Talbot plane, shifted by half a period with respect to the mask structures [15]. Scanning electron microscope (SEM) micrographs are depicted in Fig. 7 for triangular and quadratic shapes. The mask features are reliably replicated, with corner rounding arising from

Optics EXPRESS

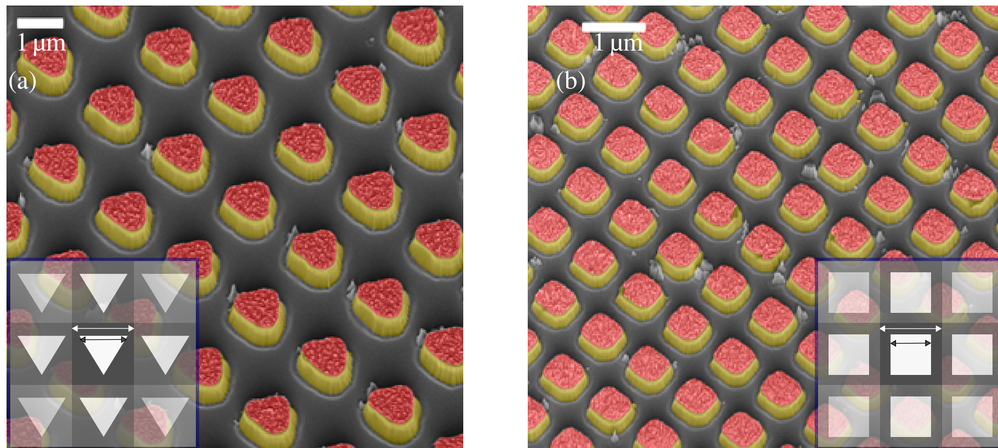

Fig. 7. Colorized SEM images of (a) triangular and (b) quadratic structures (yellow), etched into Si. The images are taken under an angle of 30°. The chromium hardmask (colored in red) used for etching is not yet removed, and the etch depth amounts to about 800 nm. The insets show a sketch of the structures on the amplitude mask, with the white areas transparent to the illumination. The size of one unit cell is $\Lambda = 1.97$ µm (white arrows), and the side lengths of the triangles and squares are 1.20 µm (black arrows). The fabricated triangular structures in (a) possess an corner radius of ~ 300 nm and a side length of 1.60 µm. The square structures in (b) have an corner radius of ~ 90 nm and a side length of 1.19 µm. While the triangular structures have slightly grown in size, the size of the square structures fits well to the design.

higher harmonics not contributing to the image formation [large $\mathbf{n}$ in Eqs. (3) and (6)] [12].

For circular patterns, we demonstrate arrays with a period of 1.39 µm [$m = 1$ in Eq. (8), compare Fig. 1(b)]. Figure 8(a) shows the resist of the print after chromium deposition, and Fig. 8(b) the structure after RIE. Here, the slanted shape of the micropillars' sidewalls arises from the etching process in use. A higher aspect ratio can be achieved by deploying a deep reactive-ion etching (DRIE) technology, for example the Bosch process. For comparison, to obtain structures with the same period using the Talbot effect under canonical i-line mask-aligner illumination, the proximity gap would have to be halved, to a value of about 10 µm [compare Fig. 1(b)].

5.3. Higher Talbot plane

Furthermore, we demonstrate Talbot lithography printing in higher Talbot planes [$m > 1$ in Eq. (8)]. Such an approach has the following advantage: The period can be reduced, i.e., a higher resolution is achieved, while at once the proximity gap can be increased with respect to the first Talbot plane. This is also indicated in Fig. 1(b): For a period of 0.71 µm, the Talbot distance at a wavelength of 193 nm corresponds to about 5 µm. By printing in the fourth Talbot plane, the original proximity gap of 20 µm can be maintained.

It is important to note once more that we rely on the Talbot effect with a 1:1 mapping between mask structures and printed patterns. We added dedicated structures to the photomask for printing in higher Talbot planes, with periods of $\Lambda_2 = 0.99$ µm, $\Lambda_3 = 0.81$ µm, and $\Lambda_4 = 0.71$ µm. One advantage of this approach becomes evident: different well-defined periods can be printed at the same fixed proximity gap of $g = 20$ µm. This is particularly important for metasurfaces relying on a tunable period, as introduced in [45].

We show SEM images of resist structures in the second, third, and fourth Talbot plane in Fig. 9. This corresponds to periods down to $\Lambda_4 = 0.71$ µm, with a diameter of ∼ 0.5 µm. For the second Talbot plane, the openings are developed through the resist to the substrate. The arrays in the third and fourth Talbot plane are not open, and consequently a lift-off process is not applicable. This issue arises from a decreasing contrast in higher Talbot planes.

The reduced quality in the higher Talbot planes has three reasons. First, due to the smaller period of the structures, higher orders carrying information about fine structures become evanescent and will not contribute to image formation in the mask plane. Second, the Talbot effect relies on plane-wave illumination. As discussed before, we achieve near plane-wave illumination, but small finite angles remain. This leads to a lateral blur of the image, most severely in large distance to the photomask, as demonstrated and discussed in connection with Fig. 5. And third, the DOF reduces with decreasing period [compare Fig. 1(b)], rendering the process more susceptible to small variations in the proximity gap. Further optimization is required with regard to the exposure dose and the use of a bottom anti-reflective coating (BARC), as discussed in Section 4.

6. Conclusion

In summary, Talbot lithography using a frequency-quadrupled laser source, with emission in the deep ultraviolet at 193 nm, provides a viable route to micro- and nanofabrication of periodic arrays in proximity lithography with superior resolution with respect to standard mask-aligner lithography. The high brilliance of the source and the monomodal operation enable efficient laser beam shaping, here demonstrated by integrating a rotating shaped random diffuser and an imaging homogenizer. The crossed arrangement of cylindrical microlens arrays in combination with a macroscopic Fourier lens leads to a uniform field distribution in the mask plane, covering a field size of 15 mm x 15 mm. The angular spectrum is controlled by inserting an aperture directly in front of the first microlens array, ensuring near plane wave illumination with half-angles below 1°.

We discussed the benefits of reducing the wavelength in Talbot lithography compared to canonical light sources, namely, a smaller period of the features and increased depth of focus

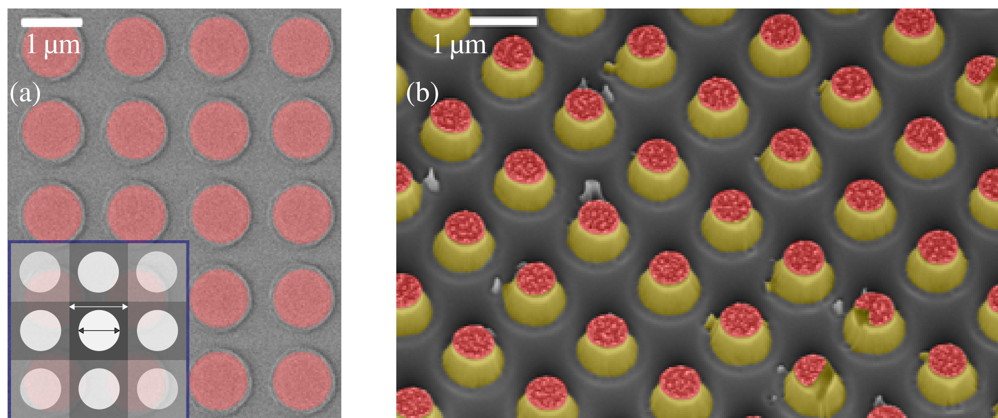

Fig. 8. Colorized SEM micrographs of (a) resist and (b) etched Si micropillars, taken under an angle of 30°. The resist openings in (a) (colored in red) correspond to the chromium hardmask in (b). The inset in (a) shows the design of the unit cell of the amplitude mask, with a period of $\Lambda = 1.4$ µm (white arrow) and a diameter of 0.8 µm (black arrow).

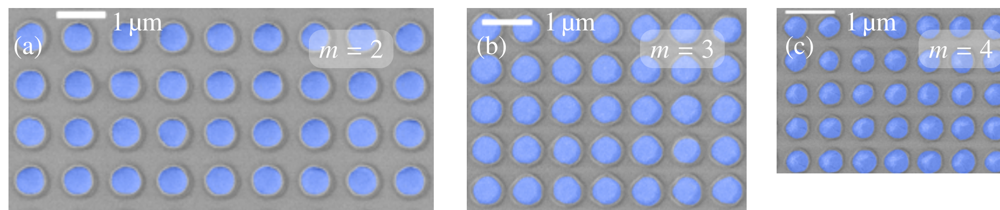

Fig. 9. Colorized SEM micrographs of periodic arrays in the photoresist, patterned in the (a) second, (b) third, and (c) fourth Talbot plane. The corresponding periods are $\Lambda_2 = 0.99\,\mu\text{m}$, $\Lambda_3 = 0.81\,\mu\text{m}$, and $\Lambda_4 = 0.71\,\mu\text{m}$, respectively. While the openings (blue) for the second Talbot plane are fully open after development, in the third and fourth Talbot plane the structures are not developed through.

at a fixed proximity gap. This improves the resolution and likewise renders the technique less susceptible to variations of the proximity gap, enlarging the process window for successful lithographic prints.

Relying on this concept, we presented the simulation and experimental results of lithographic prints at a fixed proximity gap of 20 µm. Taking the exposure wavelength into account, this translates to a period of about 1.4 µm in the first Talbot plane. By patterning a chromium hardmask and subsequent reactive-ion etching in silicon, we prove the suitability of our process for patterning periodic arrays of micropillars, as required in modern nanophotonic applications like, for example, optical metasurfaces.

Moreover, a further reduction of the period is introduced by exploiting the Talbot effect of higher order, while keeping the proximity gap fixed. Images of exposed hole arrays in the second, third, and fourth Talbot plane confirm the feasibility of the concept, with a period down to about 700 nm. However, further improvements regarding exposure irradiance and contrast are necessary for its implementation in high-volume fabrication.

Further improvements in the resolution and the process window of Talbot lithography can be expected from the combination of the presented continuous wave optical setup with rigorously optimized phase-shift masks [46], with double patterning [47], with immersion Talbot lithography [17], or with Talbot displacement lithography [16, 48].

Our studies show the applicability of Talbot lithography using a frequency-quadrupled laser source emitting at 193 nm for the manufacturing of periodic arrays, required for example for the fabrication of membranes, filters, and metastructures. Relying on a continuous wave diode laser has manifold advantages over canonical light sources in the deep ultraviolet in terms of efficiency, brilliance, and environmental sustainability.

Funding

German Federal Ministry of Research (BMBF) KMU-innovativ program, grant UVMOPA (FKZ13N13022); H2020 Marie Skłodowska-Curie Actions (MSCA) (675745); Karlsruhe School of Optics and Photonics (KSOP).

Acknowledgments

The authors want to thank M. Eisner, S. Tournois, and J. Béguelin for useful discussions and technical support. We acknowledge GenISys GmbH, Munich, Germany for the provision of the simulation software. This project has received funding from the European Union's Horizon 2020 research and innovation programme under the Marie Skłodowska-Curie grant

agreement No 675745. TOPTICA's work on this project was supported by the German Federal Ministry of Research (BMBF) by a grant under the KMU-innovativ program UVMOPA (FKZ: 13N13022). A. V. acknowledges support by the Karlsruhe School of Optics and Photonics (KSOP). Furthermore, we thank R. Li, X. Wang, and L. Liu. for the preparation of KBBF crystals.

References and links

1. L. Stuerzebecher, F. Fuchs, U. D. Zeitner, and A. Tuennermann, "High-resolution proximity lithography for nano-optical components," Microelectron. Eng. **132**, 120–134 (2015).
2. R. Völkel, U. Vogler, A. Bramati, T. Weichelt, L. Stuerzebecher, U. D. Zeitner, K. Motzek, A. Erdmann, M. Hornung, and R. Zoberbier, "Advanced mask aligner lithography (AMALITH)," Proc. SPIE **8326**, Optical Microlithography XXV, 83261Y (2012).
3. P. Rai-Choudhury, ed., *Handbook of microlithography, micromachining, and microfabrication*, vol. 1 of *IEE materials & devices series ; SPIE Press monograph* (SPIE Optical Engineering, Bellingham, Wash., 1997).
4. S. Partel, S. Zoppel, P. Hudek, A. Bich, U. Vogler, M. Hornung, and R. Voelkel, "Contact and proximity lithography using 193nm excimer laser in mask aligner," Microelectron. Eng. **87**, 936–939 (2010).
5. T. Asayama, Y. Sasaki, T. Nagashima, A. Kurosu, H. Tsushima, T. Kumazaki, K. Kakizaki, T. Matsunaga, and H. Mizoguchi, "Power up: 120 Watt injection-locked ArF excimer laser required for both multi-patterning and 450 mm wafer lithography," Proc. SPIE **8683**, Optical Microlithography XXVI, 86831G (2013).
6. M. K. Yapici and I. Farhat, "UV-LED exposure system for low-cost photolithography," Proc. SPIE **9052**, Optical Microlithography XXVII, 90521T (2014).
7. T. Weichelt, Y. Bourgin, and U. D. Zeitner, "Mask aligner lithography using laser illumination for versatile pattern generation," Opt. Express **25**, 20983–20992 (2017).
8. J. Bernasconi, T. Scharf, U. Vogler, and H. P. Herzig, "High-power modular LED-based illumination systems for mask-aligner lithography," Opt. Express **26**, 11503–11512 (2018).
9. R. Kirner, A. Vetter, D. Opalevs, C. Gilfert, M. Scholz, P. Leisching, T. Scharf, W. Noell, C. Rockstuhl, and R. Voelkel, "Mask-aligner lithography using a continuous-wave diode laser frequency-quadrupled to 193 nm," Opt. Express **26**, 730–743 (2018).
10. H. Talbot, "LXXVI. Facts relating to optical science. No. IV," Philos. Mag. Ser. 3 **9**, 401–407 (1836).
11. L. Rayleigh, "XXV. On copying diffraction-gratings, and on some phenomena connected therewith," Philos. Mag. Ser. 5 **11**, 196–205 (1881).
12. K. Patorski, *The Self-Imaging Phenomenon and its Applications*, vol. 27 of *Progress in Optics* (Elsevier, 1989).
13. H. Dammann, G. Groh, and M. Kock, "Restoration of faulty images of periodic objects by means of self-imaging," Appl. Opt. **10**, 1454–1455 (1971).
14. K. Kodate, T. Kamiya, H. Takenaka, and H. Yanai, "Construction of photolithographic phase gratings using the Fourier image effect," Appl. Opt. **14**, 522–525 (1975).
15. A. Isoyan, F. Jiang, Y. C. Cheng, F. Cerrina, P. Wachulak, L. Urbanski, J. Rocca, C. Menoni, and M. Marconi, "Talbot lithography: Self-imaging of complex structures," J. Vac. Sci. & Technol. B **27**, 2931–2937 (2009).
16. H. H. Solak, C. Dais, and F. Clube, "Displacement Talbot lithography: a new method for high-resolution patterning of large areas," Opt. Express **19**, 10686–10691 (2011).
17. T. Sato, "Talbot effect immersion lithography by self-imaging of very fine grating patterns," J. Vac. Sci. & Technol. B **30**, 06FG02 (2012).
18. D. Thomae, J. Maaß, O. Sandfuchs, A. Gatto, and R. Brunner, "Flexible mask illumination setup for serial multipatterning in Talbot lithography," Appl. Opt. **53**, 1775–1781 (2014).
19. J. T. Winthrop and C. R. Worthington, "Theory of Fresnel images I: Plane periodic objects in monochromatic light*," J. Opt. Soc. Am. **55**, 373–381 (1965).
20. W. D. Montgomery, "Self-imaging objects of infinite aperture," J. Opt. Soc. Am. **57**, 772–778 (1967).
21. J. W. Goodman, *Introduction to Fourier Optics* (Roberts & Company Publishers, 2005), 3rd ed.
22. G. C. Sherman, "Application of the convolution theorem to Rayleigh's integral formulas," J. Opt. Soc. Am. **57**, 546–547 (1967).
23. M. Born and E. Wolf, *Principles of Optics* (Cambridge University, Cambridge, UK, 1999), 7th ed.
24. T. Sato, "Focus position and depth of two-dimensional patterning by Talbot effect lithography," Microelectron. Eng. **123**, 80–83 (2014).
25. M. Scholz, D. Opalevs, P. Leisching, W. Kaenders, G. Wang, X. Wang, R. Li, and C. Chen, "A bright continuous-wave laser source at 193 nm," Appl. Phys. Lett. **103**, 051114 (2013).
26. D. Opalevs, M. Scholz, J. Stuhler, C. Gilfert, L. J. Liu, X. Y. Wang, A. Vetter, R. Kirner, T. Scharf, W. Noell, C. Rockstuhl, R. K. Li, C. Chen, R. Voelkel, and P. Leisching, "Semiconductor-based narrow-line and high-brilliance 193-nm laser system for industrial applications," Proc. SPIE **10511**, Solid State Lasers XXVII: Technology and Devices, 105112C (2018).
27. R. W. P. Drever, J. L. Hall, F. V. Kowalski, J. Hough, G. M. Ford, A. J. Munley, and H. Ward, "Laser phase and frequency stabilization using an optical resonator," Appl. Phys. B **31**, 97–105 (1983).

28. T. Saito, T. Matsunaga, K.-I. Mitsuhashi, K. Terashima, T. Ohta, A. Tada, T. Ishihara, M. Yoshino, H. Tsushima, T. Enami, H. Tomaru, and T. Igarashi, "Ultranarrow-bandwidth 4-kHz ArF excimer laser for 193-nm lithography," Proc. SPIE **4346**, Optical Microlithography XIV, 1229 (2001).
29. F. M. Dickey and T. E. Lizotte, *Laser Beam Shaping Applications* (CRC, 2017).
30. F. M. Dickey, ed., *Laser Beam Shaping: Theory and Techniques* (CRC, 2017).
31. R. Voelkel and K. J. Weible, "Laser beam homogenizing: limitations and constraints," Proc. SPIE **7102**, Optical Fabrication, Testing, and Metrology III, 71020J (2008).
32. J. W. Goodman, *Speckle Phenomena in Optics : Theory and Applications* (Roberts & Company Publishers, 2007).
33. R. Kirner, A. Vetter, D. Opalevs, M. Scholz, P. Leisching, T. Scharf, W. Noell, C. Rockstuhl, and R. Voelkel, "Enabling proximity mask-aligner lithography with a 193nm CW light source," Proc. SPIE **10587**, Optical Microlithography XXXI, 105871F (2018).
34. A. Bich, J. Rieck, C. Dumouchel, S. Roth, K. J. Weible, M. Eisner, R. Voelkel, M. Zimmermann, M. Rank, M. Schmidt, R. Bitterli, N. Ramanan, P. Ruffieux, T. Scharf, W. Noell, H.-P. Herzig, and N. De Rooij, "Multifunctional micro-optical elements for laser beam homogenizing and beam shaping," Proc. SPIE **6879**, Photon Processing in Microelectronics and Photonics VII, 68790Q (2008).
35. R. Voelkel, U. Vogler, A. Bich, K. J. Weible, M. Eisner, M. Hornung, P. Kaiser, R. Zoberbier, and E. Cullmann, "Illumination system for a microlithographic contact and proximity exposure apparatus," European Patent 2 253 997 A2 (2009).
36. A. Vetter, R. Kirner, D. Opalevs, M. Scholz, P. Leisching, T. Scharf, W. Noell, C. Rockstuhl, and R. Voelkel, "Mask-aligner Talbot lithography using a 193 nm CW light source," Proc. SPIE **10587**, Optical Microlithography XXXI, 105870W (2018).
37. MO Exposure Optics® Technical Datasheet, www.suss.com/brochures-datasheets/mo-exposure-optics.pdf.
38. LayoutLAB V4.8, 3D Proximity Lithography Simulation, www.genisys-gmbh.de.
39. J. Korka, "Standing waves in photoresists," Appl. Opt. **9**, 969–970 (1969).
40. C. A. Mack, "Analytical expression for the standing wave intensity in photoresist," Appl. Opt. **25**, 1958–1961 (1986).
41. C. Mack, *Fundamental Principles of Optical Lithography* (John Wiley & Sons, Ltd, Chichester, UK, 2007).
42. K. E. Chong, I. Staude, A. James, J. Dominguez, S. Liu, S. Campione, G. S. Subramania, T. S. Luk, M. Decker, D. N. Neshev, I. Brener, and Y. S. Kivshar, "Polarization-independent silicon metadevices for efficient optical wavefront control," Nano Lett. **15**, 5369–5374 (2015).
43. M. Decker, I. Staude, M. Falkner, J. Dominguez, D. N. Neshev, I. Brener, T. Pertsch, and Y. S. Kivshar, "High-efficiency dielectric Huygens' surfaces," Adv. Opt. Mater. **3**, 813–820 (2015).
44. S. Liu, A. Vaskin, S. Campione, O. Wolf, M. B. Sinclair, J. Reno, G. A. Keeler, I. Staude, and I. Brener, "Huygens' metasurfaces enabled by magnetic dipole resonance tuning in split dielectric nanoresonators," Nano Lett. **17**, 4297–4303 (2017).
45. K. E. Chong, L. Wang, I. Staude, A. R. James, J. Dominguez, S. Liu, G. S. Subramania, M. Decker, D. N. Neshev, I. Brener, and Y. S. Kivshar, "Efficient polarization-insensitive complex wavefront control using Huygens' metasurfaces based on dielectric resonant meta-atoms," ACS Photonics **3**, 514–519 (2016).
46. Y. Bourgin, T. Käsebier, and U. D. Zeitner, "250 nm period grating transferred by proximity i-line mask-aligner lithography," Opt. Lett. **39**, 1665–1668 (2014).
47. Y. Bourgin, D. Voigt, T. Käsebier, T. Siefke, E.-B. Kley, and U. D. Zeitner, "175 nm period grating fabricated by i-line proximity mask-aligner lithography," Opt. Lett. **42**, 3816–3819 (2017).
48. H. H. Solak, C. Dais, F. Clube, and L. Wang, "Phase shifting masks in displacement Talbot lithography for printing nano-grids and periodic motifs," Microelectron. Eng. **143**, 74–80 (2015).